RSC Pharmaceutics

ROYAL SOCIETY OF CHEMISTRY

PAPER

View Article Online
View Journal | View Issue

Open Access Article. Published on 20 October 2025. Downloaded on 4/3/2026 6:48:24 AM.
This article is licensed under a Creative Commons Attribution-NonCommercial 3.0 Unported Licence.

Check for updates

Cite this: *RSC Pharm.*, 2026, **3**, 117

The ideal duo for salt formation: vinpocetine and tosylic acid

Ilenia D'Abbrunzo,[a] Francesca Beltrame,[a] Lara Gigli,[b] Nicola Demitri,[b] Cinzia Cepek,[c] Ferdinando Bassato,[c] Giuseppe Procida,[a] Dario Voinovich[a] and Beatrice Perissutti*[a]

Received 25th August 2025,
Accepted 9th October 2025

DOI: 10.1039/d5pm00225g

rsc.li/RSCPharma

Two novel soluble salts of vinpocetine were prepared through simple and highly sustainable mechanochemical methods. Specifically, water-assisted grinding led to the formation of a crystalline, anhydrous, equimolar salt with *p*-toluenesulfonic acid, whereas neat grinding produced its amorphous counterpart. The structure of the crystalline salt was elucidated using single-crystal X-ray diffraction, while the ionic nature of the amorphous salt was confirmed by X-ray photoelectron spectroscopy. The large ΔpK_a between *p*-toluenesulfonic acid and vinpocetine promotes the formation of a stable salt, with strong ionic interactions between the protonated tertiary amine of vinpocetine and the tosylate anion (as also attested by amorphous salt glass transition of about 81 °C). Both salts significantly enhance the saturation solubility of vinpocetine at 37 °C in phosphate buffer, achieving thermodynamic equilibrium in half the time compared to the pure crystalline drug. These findings highlight new opportunities for the development of vinpocetine, a compound with well-documented effects on cerebral circulation, whose broader application has so far been limited by its extremely low aqueous solubility.

1. Introduction

Successful salt formation, typically requiring a pK_a difference of 3–4 units between the protonated base and the acid, is a well-established strategy for improving the physicochemical properties of ionizable active pharmaceutical ingredients (APIs).[1] The well-known benefits of salt formation include enhanced dissolution rates, improved solid-state properties, and higher melting points compared to the free base.[2] For amorphous drugs, salt formation can reduce the tendency for recrystallization by increasing the glass transition (T_g). Furthermore, salt formation has been shown to impact recrystallization tendencies, as recrystallization temperatures of amorphous salts are typically higher than those of the free base.[3]

The conventional salt formation of ionizable pharmaceutical bases involves an acid–base reaction, where a weak base reacts with an acid to form a salt. This process includes several steps, such as preparing the base solution in an appropriate solvent, gradually adding the chosen acid to protonate the base, adjusting the pH to ensure complete salt formation, and finally isolating and purifying the salt through crystallization or solvent evaporation.[4] In contrast, mechanochemical salt formation of a weak base uses mechanical techniques – such as grinding – to drive an acid–base reaction without the use of a solvent. The process typically consists of a single step, in which the weak base and a suitable acid – selected according to the same criterion, namely its ability to protonate the base – are mixed in their solid powder forms, usually using a mortar or a ball mill.[1,5] Under appropriate conditions, the energy generated during the milling process promotes the protonation of the base by the acid, resulting in salt formation. This approach offers the added advantage of eliminating the need for subsequent salt purification.

The subject of this study, vinpocetine (Fig. 1) (hereinafter referred to as VINPO), is a semisynthetic derivative of the natural alkaloid vincamine, introduced to the market in 1978 and employed in the treatment of ischemic stroke and other cerebrovascular disorders.[6–8] Its global demand is expected to grow, driven by population aging and the increasing prevalence of stroke. Although vinpocetine shows no significant side effects, toxicities, or contraindications at therapeutic dose, its clinical utility is greatly limited by its low bioavailability (~6.7%),[9] primarily due to its poor aqueous solubility[10] and extensive hepatic first-pass metabolism.[7] The pK_a value of vinpocetine is approximately 7.3,[11] and the compound

---

[a] *Department of Chemical and Pharmaceutical Sciences, University of Trieste p.le Europa 1, 34127 Trieste, Italy. E-mail: bperissutti@units.it*
[b] *Elettra-Sincrotrone Trieste, S.S. 14 Km 163.5 in Area Science Park, Basovizza, Trieste, Italy*
[c] *CNR – Istituto Officina dei Materiali (IOM), 34149 Basovizza, Trieste, Italy*

© 2026 The Author(s). Published by the Royal Society of Chemistry

Open Access Article. Published on 20 October 2025. Downloaded on 4/3/2026 6:48:24 AM.
This article is licensed under a Creative Commons Attribution-NonCommercial 3.0 Unported Licence.

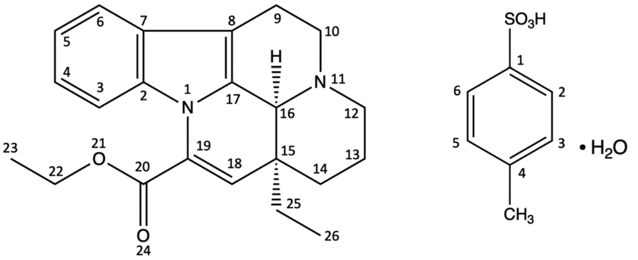

Fig. 1 (left) Vinpocetine and (right) *p*-toluenesulfonic acid monohydrate molecular structures with atom numbering.

has a well-documented ability to form salts with various acids, which will be discussed in more detail below. Moreover, while vinpocetine does not exhibit polymorphism, it has shown a remarkable tendency to form amorphous phases, including solid dispersions and amorphous salt forms. Therefore, in this context, the present study aims to enhance vinpocetine solubility by developing both crystalline and amorphous salts using mechanochemistry as a synthesis technique.

Aside from a vinpocetine ionic cocrystal, obtained through classical slow evaporation,[12] and the citrate salt patented under the name Oxopocetine, and two salts with inorganic salt (perchlorate and phosphate salts of VINPO) also obtained by solution crystallization,[13] the literature reports few examples of VINPO salts obtained by mechanochemistry. Among these, a VINPO salt with citric acid was obtained *via* mechanochemical activation in the presence of polymers (crosslinked polyvinylpyrrolidone) using a planetary mill,[14] yielding an amorphous salt with a markedly enhanced dissolution rate compared to the free base. Similarly, VINPO combined with oxalic acid was shown to form either an amorphous or a crystalline hydrogenoxalate salt, depending on whether neat grinding or liquid-assisted grinding was employed.[15]

More recently, VINPO has also been converted into a salt using a vibrational mill with malic acid, exhibiting notable enantioselectivity[11] and yielding either an amorphous or crystalline salt depending on the enantiomeric form of the coformer.

In this study, neat grinding (NG) and water-assisted grinding (WAG) were employed to obtain two salt forms of vinpocetine, exhibiting either amorphous or crystalline characteristics. The coformer used in this multicomponent system is *p*-toluenesulfonic acid (hereinafter referred to as PTOS) (Fig. 1), a strong organic acid with a pK_a of −1.34 in water.[16,17] Unlike many inorganic acids, PTOS is a solid at room temperature (as a monohydrate), non-oxidizing, and easy to handle. It is considered eco-friendly, cost-effective, and non-toxic, though it may cause irritation to skin and eyes. Thanks to its strong acidity, PTOS acts as an efficient catalyst and readily forms salts and hydrogen bonds, enabling a wide range of interactions and cocrystal formation. Despite the growing interest in its organic counterions for their stability in aqueous pharmaceutical formulations, PTOS remains underexplored in the field of mechanochemistry.

2. Materials and methods

2.1 Materials

Vinpocetine (VINPO, Linnea SA, Riazzino, Locarno, Switzerland, indexed as LAGZOI in the Cambridge Structural Database (CSD))[18] and *p*-toluenesulfonic acid monohydrate (PTOS MH, Sigma-Aldrich Ltd, St Louis, USA) were used without further purification, while water (H_2O) was freshly distilled water. KH_2PO4 and NaOH of analytical grade, and ethylacetate (EA), hexane (HXN), 4-methyltetrahydropyran (4-MTHP), acetone (ACT), methanol (MeOH), ethanol (EtOH), acetonitrile (ACN) and ammonium acetate (AmAc) HPLC-grade were purchased by Sigma-Aldrich Ltd (St Louis, USA).

2.2 Samples preparation

2.2.1 Mechanochemical salt formation. A Retsch Mill MM400 (Retsch, Germany) and two stainless steel jars equipped with screw closure (internal volume of 25 mL), were used for milling experiments. The grinding media consisted of one 10 mm ∅ stainless steel ball. For each mechanochemical experiment, the amount of VINPO – PTOS MH equimolar mixture was kept fixed at 400 mg. For obtaining (*via* NG) the amorphous salt, the milling frequency and time were kept fixed at 25 Hz and 240 minutes, respectively. For crystallizing (by WAG) the crystalline salt, the milling frequency and time were kept fixed at 25 Hz and 120 minutes, respectively, and 160 mL of H_2O were added prior to milling directly into the milling jars, using Eppendorf Research plus micropipettes (Eppendorf, Hamburg, Germany). To ensure reproducibility, each experiment was performed at least in duplicate. The mechanochemical products were characterized by powder X-ray diffraction (PXRD) and differential scanning calorimetry (DSC) the day after their preparation.

2.2.2 Salt formation by solution crystallization. A single crystal of appropriate size for single-crystal X-ray diffraction (SXRD) analysis was obtained by conventional solution crystallization, starting from preformed seeds of VINPO–PTOS adduct (obtained by WAG). Specifically, 10 mg of the preformed VINPO–PTOS salt was dissolved in 4 mL of EA into a 7 mL Snap/Clip Top Vial. The suspension was stirred at room temperature for approximately one hour. The vial containing the solution was sealed with parafilm, punctured with two holes, and left under a fume hood until complete solvent evaporation at room temperature. Single crystals appeared after 15 days.

2.3 Samples characterization

2.3.1 Powder X-ray diffraction (PXRD). For PXRD measurements, a Bruker D2 Phaser diffractometer (Bruker, Manheim, Germany) with Cu-Kα source (λ = 1.54 Å) was used. The system works with a 300 W low power X-ray generator (30 kV at 10 mA). The steel sample holder used has a capacity of 300 μL, while cylindrical gearboxes in polyvinylidene fluoride (PVDF) were using for reducing the capacity to about 100 μL of solid. The conditions used for the measurement were as follows: 2θ

© 2026 The Author(s). Published by the Royal Society of Chemistry

Open Access Article. Published on 20 October 2025. Downloaded on 4/3/2026 6:48:24 AM. This article is licensed under a Creative Commons Attribution-NonCommercial 3.0 Unported Licence.

angles from 3° to 40°, 0.02° 2θ increment, time step 0.6 seconds.

2.3.2 Synchrotron X-ray diffraction analysis – structural characterization of the crystalline salt. Data collections of both the powder and the single crystal of the crystalline salt were performed at the XRD2 beamline of the Elettra Synchrotron, Trieste (Italy).[19] Crystals have been dipped in NHV oil (Jena Bioscience, Jena, Germany) and mounted on the goniometer head with Kapton loops (MiTeGen, Ithaca, USA). Complete datasets were collected through the rotating crystal method, at 100 K and 298 K (using a nitrogen stream, supplied through an Oxford Cryostream 700). The single crystal data were acquired using monochromatic wavelength of 0.620 Å on Pilatus 6 M hybrid-pixel area detectors (DECTRIS Ltd, Baden-Daettwil, Switzerland). The powder sample of the salt was measured at 298 K in transmission mode filling a boron capillary of 0.3 mm of diameter. Synchrotron powder data were acquired for the crystalline sample (obtained by WAG) using monochromatic wavelength of 1.00 Å on the same area detector. The two-dimensional powder pattern has been integrated using GSASII program,[20] after preliminary calibration of hardware setup, using a capillary filled with LaB_6 standard reference powder (NIST 660a).

The single crystal diffraction data were indexed, integrated and scaled using XDS.[21] The structures were solved by the dual space algorithm implemented in the SHELXT code.[19] Fourier analysis and refinement were performed by the full-matrix least-squares methods based on F2 implemented in SHELXL (Version 2019/3).[19] The Coot program was used for modeling.[22] Anisotropic thermal motion refinement has been used for all atoms with full occupancies. Refined Flack parameters[23] confirm the expected stereocenter configurations (*S*). Pictures were prepared using Ortep-3,[24] and CCDC Mercury software.[25]

CCDC numbers 2447789 and 2447790 contain the supplementary crystallographic data for the salt crystals at 100 K and 298 K, respectively.

2.2.3 X-ray photoelectron spectroscopy (XPS). All XPS spectra were acquired at room temperature in normal emission geometry using a conventional Mg Kα X-ray source ($h\nu$ = 1253.6 eV) and a 120° hemispherical electron energy analyzer (overall energy resolution: about 0.8 eV). The binding energy scale has been calibrated by fixing the C 1s photoemission line due to hydrocarbon to 284.6 eV. All spectra were normalized to the incident photon flux and were analyzed by performing a non-linear mean square fit of the data with a Levenberg–Marquardt algorithm after a Shirley background removal. The experimental data were fitted with a Voigt line shape where the Lorentzian width was set to 0.4/0.5 eV and the Gaussian one left as a free parameter, but equal for all components: the fitting details are reported in Tables S1–S3 in the SI file.

2.2.4 Drug recovery. VINPO quantification was performed using a HPLC method adapted from VINPO monograph in the Eur. Ph. (Ed. 11.0)[10] and validated following a minor adjustment to the column length. The HPLC system used consisted of Quaternary Pump VL GT 111A (1260 Infinity II, Agilent Technologies, U.S.A.), a UV–DAD (GT 115 A, Agilent Technologies, U.S.A.), an autosampler (GT 125 A Vial sampler, Agilent Technologies, U.S.A.), an interface (Chem Station, OpenLAB CDS, Agilent Technologies, U.S.A.) for the acquisition of data. The mobile phase comprised of 15.4 g L^{-1} solution of ammonium acetate *R*, acetonitrile *R* (45 : 55 V/V), the flow rate was 1 mL min^{-1} and absorbance readings were conducted at fixed wavelength of 280 nm. A BDS hypersil C18 250 × 4.6 mm, 5 µm column (Thermo Scientific, U.S.A.) was used. Analyses were performed at room temperature. The retention time of VINPO was 14.52 min and the run time was set at 20 min. Quantification was carried out by integration of the peak areas using the external standardization method. Under these conditions, the linear calibration curve of VINPO was obtained in the range of 0.125–1 mg mL^{-1} (r^2 = 0.9992). As reference solution, the standard of the day was prepared each time before starting the analysis. The standard solution was prepared by dissolving about 10 mg, exactly weighed, of VINPO in 50 mL of mobile phase. The solution was stirred for several minutes and then 1 : 10 and 1 : 20 dilutions with the mobile phase were prepared to obtain a drug concentration of approximately 2.5 mg L^{-1}. According to the VINPO monograph in the Eur. Ph., specified impurities, named impurities A, D, B and C have relative retention (with reference to VINPO) of 0.4, 0.68, 0.75 and 0.83, respectively. The determination of the VINPO content and eventually of the related impurities into the salt samples was determined by dissolving about 10 mg, exactly weighed, of sample in 50 mL of mobile phase. In the sample solution of each multicomponent system, the retention time of the major peak was the same as VINPO, *i.e.*, 14.52 min. Each sample solution was analyzed in triplicate.

2.2.5 Differential scanning calorimetry (DSC) analysis. For DSC analysis, each sample weighing 2–4 mg was introduced into an aluminum sealed and pierced 40 µL crucible and analyzed by a Mettler Toledo DSC 3 Star System (Milan, Italy) with a heating program of 30–225 °C (10 °C min^{-1}) under a nitrogen (N_2) atmosphere (50 mL min^{-1} flow rate). Melting temperatures (mean of at least three replicates) are reported as peak temperatures. The following samples were analyzed: pure VINPO and PTOS MH, amorphous salt and crystalline salt and a selection of aged samples.

To obtain the T_g of PTOS MH and the amorphous salt (expressed as the mean inflection point on the reheating thermal curve), DSC heating–cooling–heating cycles were performed. These cycles were performed under a nitrogen (N_2) flow of 50 mL min^{-1}, following this protocol: (1) heating from 30 °C to 225 °C at a rate of 10 °C min^{-1}; (2) isotherm at 225 °C for 5 min; (3) cooling from 225 °C to −30 °C at a rate of 50 °C min^{-1}; (4) isotherm at −30 °C for 5 min; (5) re-heating from −30 °C to 225 °C at a rate of 40 °C min^{-1}.

2.2.6 Thermogravimetric analysis (TGA). TGA analyses of crystalline and amorphous salt were performed using a Mettler Toledo TGA 2 (Milan, Italy). Briefly, 5–10 mg of the powdered sample were inserted into Alumina 100 µL crucibles and analyzed with a heating program of 30–300 °C (10 °C min^{-1}) under a nitrogen (N_2) atmosphere (50 mL min^{-1} flow rate).

© 2026 The Author(s). Published by the Royal Society of Chemistry

Open Access Article. Published on 20 October 2025. Downloaded on 4/3/2026 6:48:24 AM.
This article is licensed under a Creative Commons Attribution-NonCommercial 3.0 Unported Licence.

2.2.7 Fourier-transform infrared spectroscopy (FT-IR) analysis. Powdered samples (pure VINPO and PTOS MH, amorphous and crystalline salts) were analyzed with a Shimadzu IRAffinity-1S FT-IR instrument (Kyoto, Japan) using the attenuated total reflectance technique, in a range of 400–4000 cm^{-1} with a resolution of 4 cm^{-1} and 20 scans.

2.2.8 Solubility studies. To evaluate the solubility of the new VINPO–PTOS salts in comparison with pure VINPO, solubility tests were performed in screw-capped 15 mL glass vials by adding an excess of powder to 10 mL of KH_2PO_4/NaOH 1 M phosphate buffer (pH 7.4). Each experiment was carried out at 37 ± 0.5 °C, using a thermostatic water bath. After 1 or 2 days, samples were collected and filtered through a 0.22 µm polyethersulfone syringe membrane filter (Millex™-GP, Merck KGaA, Darmstadt, Germany). The concentration of dissolved VINPO was determined spectrophotometrically at a wavelength of 313 nm, where the UV absorption of PTOS did not interfere. At least three replicates were performed for each sample and time point.

2.2.9 Scanning electron microscopy (SEM) analysis. Images of amorphous and crystalline salts were collected through SEM and compared to those of pure individual components. The powdered samples were placed on aluminum stubs covered with a carbon double-sided tape and sputter-coated with gold using a Sputter Coater K550X (Emitech, Quorum Technologies Ltd, UK), before being analyzed by a scanning electron microscope (Quanta 250 SEM, FEI, Oregon, USA) with the secondary electron detector. The working distance was set at 10 mm to obtain the appropriate magnifications, and the acceleration voltage was set at 30 kV. VINPO and PTOS-MH were analyzed in environmental conditions (ESEM) using a Scanning Electron Microscope FEI Quanta 250, using a working distance of 10 mm and an acceleration voltage of 30.

2.2.10 Physical stability studies. The two salts were stored in sealed plastic vials within a desiccator at a constant temperature of 20 °C and monitored over a period of three months. Solid-state properties were assessed by PXRD and DSC analyses to evaluate the physical stability of the VINPO–PTOS salts.

Additionally, to assess the effect of humidity on their solid-state properties, both the crystalline and amorphous salts were placed on microscope slides in a desiccator maintained at 74% relative humidity (RH) (using a saturated NaCl solution), within the same climate-controlled room at 20 °C.

3. Results and discussion

Given the substantial pK_a difference between VINPO and PTOS (approximately 8.6), their combination represented a promising strategy for salt formation. This was successfully accomplished using a simple and sustainable mechanochemical approach, resulting in the preparation of two distinct salt forms through grinding.

On one hand, water-assisted grinding (WAG) (2 h at 25 Hz with 160 µL of freshly distilled water) resulted in a white, free-flowing powder. Beyond the obvious advantages of using water as a green, non-toxic solvent, this process led to the formation of a new crystalline phase. The PXRD pattern of the resulting solid displayed distinct and sharp peaks at 9.52°, 11.84°, 16.28°, 19.29°, and 21.01° 2θ, with no residual reflections from the starting materials (Fig. 2, green pattern), confirming both the purity of the product and the emergence of a novel solid form. The crystal structure solution and the nature of the new crystalline product (*i.e.*, salt *vs.* cocrystal character) are reported in the section below (section 3.1).

The same crystalline phase could be obtained by grinding under similar conditions in the presence of HXN, EA, 4-MTHP, ACT, EtOH, MeOH, or ACN. However, the bulk properties of these solids were less favorable, as they appeared grayish and often pasty (see Fig. S1 in the SI file) and were not always completely free of residual starting coformers, as confirmed by the PXRD pattern (Fig. S2 in the SI file).

On the other side, a simple neat grinding (NG) process carried out for 4 hours at 25 Hz – following a previously established protocol for amorphous systems preparation[26] – led to a fully white powder that was entirely amorphous, with no detectable diffraction peaks from the original crystalline VINPO or PTOS MH. PXRD analysis revealed a typical halo pattern (Fig. 2).

3.1 Determination of salt *versus* cocrystal character of the new crystalline product

A single crystal of appropriate size for SXRD analysis was then obtained by conventional solution crystallization, starting from preformed seeds of VINPO–PTOS crystalline adduct (obtained by WAG). The powder and single-crystal diffraction data collections of the VINPO–PTOS crystalline sample enabled structure solution. At 298 K, the crystals of the VINPO–PTOS adduct display 1 VINPO and 1 PTOS crystallographic independent molecules in the asymmetric unit (ASU) (Fig. 3). Salt bridges links protonated tertiary amine of VINPO and tosylate counterion (shorter –SO^{3-}···+HN– distance is 2.724(2) Å at 298 K). Data collected at 100 K confirm the same crystal form found at room temperature, with small cell volume contraction (~2%). A first overlap of the pattern simu-

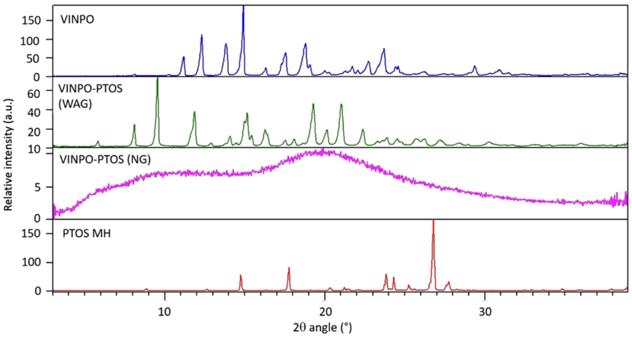

Fig. 2 PXRD pattern of VINPO–PTOS crystalline adduct (green) obtained *via* WAG and VINPO–PTOS amorphous system obtained *via* NG (purple), in comparison with the two starting materials, VINPO (blue) and PTOS MH (red).

© 2026 The Author(s). Published by the Royal Society of Chemistry

Open Access Article. Published on 20 October 2025. Downloaded on 4/3/2026 6:48:24 AM.
This article is licensed under a Creative Commons Attribution-NonCommercial 3.0 Unported Licence.

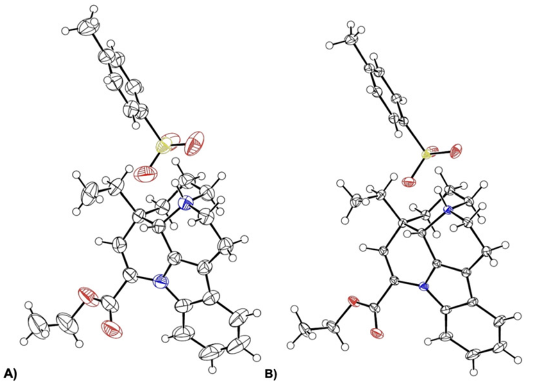

Fig. 3 Asymmetric unit of VINPO–PTOS salt at 298 K (A) and 100 K (B).

lated from the single crystal structure and the experimental powder pattern immediately highlighted a perfect correspondence. Anyway, for sake of clarity, the structure solved by the single crystal at 298 K was used as starting model for the Rietveld refinement of the powder pattern. The refinement (Fig. 4), where soft restrains on the atom distances (±0.03 Å) and angles (±0.1°) were applied, was performed in GSASII and resulted in a R-Bragg factor of 3.55%. The entire unit cell representation is shown in Fig. 4, and the essential crystallographic and refinement data are reported in Table S4 in the SI file.

3.2 Assessment of the salt nature of the amorphous VINPO–PTOS phase

Based on the confirmation that the crystalline product corresponds to vinpocetine tosylate salt, further studies were conducted to evaluate whether the amorphous phase also retained the salt character. Previous literature has already demonstrated VINPO ability to form amorphous salts, such as vinpocetine citrate[14] and vinpocetine malate.[14] In this case, the crystalline VINPO–PTOS salt (whose structure had been previously solved) was used as a reference to investigate the nature of the amorphous counterpart. To this end, XPS was selected, as it is a powerful technique for probing protonation states and identifying salt formation in amorphous systems. This method had already proven effective in similar studies, such as that on vinpocetine citrate.[14]

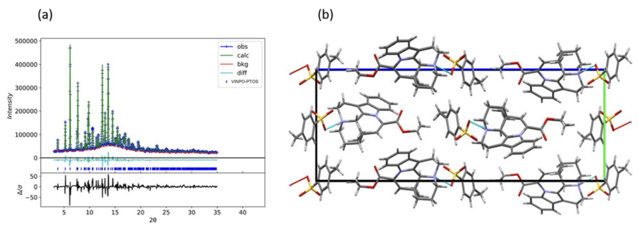

Fig. 4 (a, left) Experimental pattern (recorded using Synchrotron radiation, wavelength: 1.00 Å) (blue cross) and calculated (green line) Rietveld refinement profile fit and difference curve (cyano line) of the refined model. The residuals are displayed on the bottom in black and the reflection ticks in blue. The hump centered at 2θ = 15° is due to the capillary (sample holder) used to perform the measurement. (b, right) Crystal packing of the VINPO–PTOS adduct at 298 K viewed along the [100] direction. H-bond are represented with cyano dashed line.

Fig. 5 presents a comparison of the N 1s XPS spectra for pure VINPO (c), VINPO–PTOS amorphous phase (b), and crystalline VINPO–PTOS salt (a). Due to observed charging shifts in all measured samples, the binding energy scale was calibrated by fixing the C 1s photoemission line corresponding to hydrocarbons at 284.6 eV (spectra shown in Fig. S3, while O 1s spectra are depicted in Fig. S4 in the SI file). The N 1s spectrum of pure VINPO reveals two components, corresponding to the two inequivalent nitrogen atoms present in the molecule, N1 and N11 (see Fig. 1 for the molecular structure). Binding energies of 400.3 eV and 398.9 eV are attributed to VINPO N1 and N11, respectively. The N 1s spectrum of the VINPO–PTOS crystalline salt (red curve in Fig. 5) shows two main peaks at 400.5 eV and 401.7 eV. The lower binding energy peak corresponds, within experimental error, to N1 atoms of pure VINPO, while the higher binding energy peak corresponds to the protonated N11 nitrogen atoms. Similarly, the amorphous sample yields an N 1s spectrum closely resembling that of the crystalline form, with two components, ascribed to N1 and N11, once again clearly identifiable. These findings indicate the formation of VINPO–PTOS salt in both crystalline and amorphous samples, *via* proton transfer in a solid-state reaction, facilitated by mechanical energy.

3.3 Comprehensive characterization of the two salts

The primary objective was to evaluate the recovery of VINPO following the WAG and NG processes. Although it is well established that grinding can induce structural changes and even promote undesirable chemical transformations, such effects are seldom investigated in mechanochemical activation studies. In this context, the prolonged and intense conditions of the NG process (4 hours at 25 Hz), as well as the presence of water and a strong acid during the WAG process – factors that could potentially lead to VINPO hydrolysis[27] – were expected to

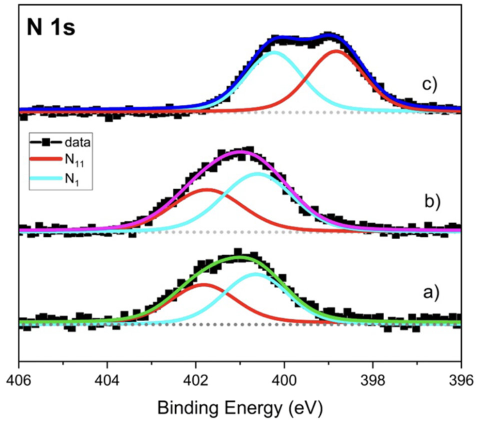

Fig. 5 Comparison of the N 1s XPS spectra for pure VINPO (c), VINPO–PTOS amorphous salt (b), and crystalline VINPO–PTOS salt (a).

Open Access Article. Published on 20 October 2025. Downloaded on 4/3/2026 6:48:24 AM.
This article is licensed under a Creative Commons Attribution-NonCommercial 3.0 Unported Licence.

significantly reduce drug recovery. However, the chromatograms revealed a high recovery rate for both samples: 97.21% ± 0.34 for the crystalline tosylate salt (WAG) and 96.91% ± 0.25 for the amorphous tosylate salt (NG), based on three replicates. The difference between the two was minimal and not statistically significant ($p > 0.05$). These findings suggest that, despite the processing conditions, neither method substantially compromises the chemical integrity of VINPO. Impurities related to VINPO were detected only in trace amounts in both salt samples, remaining below the integration threshold (representative chromatograms are presented in Fig. S5).

VINPO ESEM image (3000× magnification), consistent with previous literature reports,[28] reveals large, irregularly shaped particles accompanied by numerous smaller fragments. In contrast, PTOS MH, observed at lower magnification (200×), consists of large particles with rough, irregular surfaces – features that reflect its hygroscopic nature and tendency to deliquescence. This phenomenon, evidenced by light scattering and surface reflections, also contributes to the difficulty in achieving sharp image focus. The mechanochemical process induces a significant variation in the shape and size of the powder, resulting in both salts forming a finely grained powder with very small particle size. VINPO–PTOS crystalline salt shows well-defined, small crystalline particles with smooth surfaces at 50 000× magnification. SEM imaging clearly highlights the crystalline nature of the salt consisting of an agglomerate of tiny crystalline particles, a typical feature of materials produced by milling, which inherently reduces particle size. The amorphous salt exhibits small, smooth-surfaced particles and a larger particle size compared to the crystalline salt powder. SEM analysis confirms the existence of a single, homogeneous phase within the sample.

A comparison of ESEM and SEM images of the starting materials and the two new salts is reported in Fig. 6.

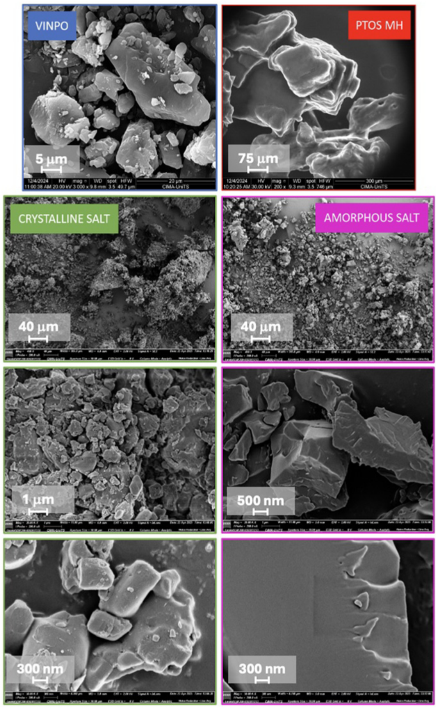

Fig. 6 ESEM images of starting VINPO (3000×) and PTOS-MH (200×), compared with SEM images of crystalline and amorphous VINPO–PTOS salts (from top to bottom: 400×, 20 000×, 50 000×). Each SEM image includes its corresponding scale bar.

The thermal parameters of VINPO, as measured at the DSC analyses, show a melting peak at 150.52 ± 0.19 °C, with an enthalpy of fusion (ΔH) of -107.06 ± 1.97 J g^{-1}. In the case of PTOS MH, the melting point is 105.17 ± 0.15 °C, with a ΔH of -243.21 ± 36.80 J g^{-1} (mean ± s.d., $n = 3$ in both starting materials). The DSC thermogram of the crystalline sample (green curve, Fig. 7) displayed a single endothermic event corresponding to its melting point, confirming its anhydrous nature. This contrasts with the starting PTOS, which is a monohydrate. No residual thermal events of the coformers were detected in the range of analysis. The salt exhibited a high melting point at 199.63 ± 0.14 °C ($\Delta H = -61.44 \pm 1.95$ J g^{-1}) (mean ± s.d., $n = 6$), significantly exceeding those of the two starting coformers (150.30 °C and 105.28 °C for VINPO and PTOS MH, respectively). TGA analysis (Fig. S6 in the SI file) supported these results, confirming the anhydrous nature of the crystalline solid and demonstrating its thermal stability up to approximately 20 °C beyond its melting point. Beyond this temperature, the salt underwent thermal decomposition, reverting to the original coformers. Notably, despite PTOS MH being a monohydrate and its known tendency to form hydrated salts,[29,30] VINPO–PTOS crystalline salt remains anhydrous.

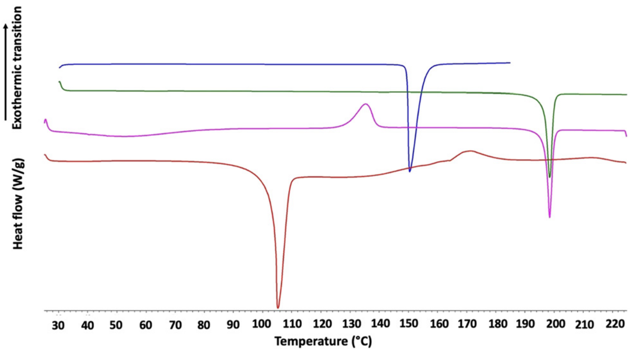

Fig. 7 DSC curves of VINPO–PTOS crystalline (green) and amorphous (purple) salts in comparison with the two starting materials: VINPO (blue) and PTOS MH (red).

The DSC curve of the amorphous salt (also depicted in Fig. 7 in purple), after a minor endothermic event corresponding to dehydration from adsorbed moisture, revealed a recrystallization event (at 131.25 ± 2.55, ΔH 41.27 ± 1.95 J g^{-1}), followed by an endothermic melting peak, which perfectly overlapped with the melting endotherm of the crystalline salt, having a m.p. at 198.02 ± 0.25 °C with an associated enthalpy of -56.45 ± 3.48 J g^{-1} (mean ± s.d., $n = 6$). TGA (Fig. S7 in the SI file) showed an initial weight loss due to the presence of

© 2026 The Author(s). Published by the Royal Society of Chemistry

Open Access Article. Published on 20 October 2025. Downloaded on 4/3/2026 6:48:24 AM.
This article is licensed under a Creative Commons Attribution-NonCommercial 3.0 Unported Licence.

adsorbed water (less than 2% by weight). Beyond this, the TGA curve of the amorphous salt closely matched that of the crystalline counterpart.

The DSC analysis, conducted through heating/cooling/heating cycles on the amorphous sample (Fig. S8), revealed a single glass transition temperature (T_g) at 80.65 ± 0.68 °C (mean ± s.d., n = 3). This confirms the presence of a single homogeneous solid phase and suggests a potentially high physical stability of the system. According to the Gordon-Taylor equation, and using the previously determined T_g of VINPO (22.81 °C)[11] and the T_g determined in this study for PTOS MH (158.21 °C, see Fig. S9) – both expressed as inflection points – the theoretical T_g for an equimolar mixture is 67.5 °C. A true density ratio of 0.955 (VINPO-to-PTOS) was applied.

Interestingly, the experimental T_g value is approximately 15 °C higher than the predicted value. This positive deviation strongly supports the existence of ionic interactions between the protonated N11 atom of the VINPO indolizidine ring and the tosylate anion. Moreover, the high T_g of the amorphous salt suggests a low tendency to recrystallize at room temperature (based on the empirical T_g – 50°K guideline).[31]

As a complementary analysis to further characterise the new vinpocetine tosylate salts, FT-IR ATR spectra were collected (Fig. S10 in the SI file). The spectra of the crystalline and amorphous salts are clearly distinguishable from those of the starting materials (VINPO and PTOS·H_2O), confirming the formation of a new solid phase. Notably, the spectra of the crystalline and amorphous forms are very similar, indicating that both share essentially the same type of intermolecular interactions. Minor differences are observed, such as the shift of the C=O stretching vibration of VINPO (from 1716 cm^{-1} in the free base[28,32,33] to 1721–1723 cm^{-1} in the salts) and the presence of broad O–H stretching bands in the amorphous form, consistent with residual moisture as confirmed by TGA.

Although VINPO initially exhibited highly variable and poorly reproducible dissolution behavior, it reached equilibrium after 48 hours, with a mean solubility of C_s = 1.28 ± 0.20 mg L^{-1} (mean ± s.d., n = 3) at 37 °C in pH 7.4 buffer, consistent with previously reported value in literature.[12] In comparison, the newly obtained VINPO–PTOS crystalline salt exhibited a higher solubility and a shorter time to reach equilibrium under the tested conditions. In particular, it reached equilibrium within just 24 hours, achieving a mean solubility of C_s = 5.37 ± 0.66 mg L^{-1} with a slight increase to 6.01 ± 0.48 mg L^{-1} after 48 hours, indicating stability over time. The amorphous VINPO–PTOS salt, upon contact with water, underwent rapid precipitation followed by crystallization into the same crystalline salt form, as confirmed by PXRD analysis of the recovered sample (see Fig. S11). As a result, its final solubility under the tested conditions was not significantly different from that of the crystalline salt, showing an approximately fourfold increase relative to pure VINPO. In particular, the (initially) amorphous salt reached a concentration of 4.67 mg L^{-1} ± 0.27 after 24 hours, which remained essentially unchanged thereafter (5.20 ± 0.47 mg L^{-1}). After the solubility test, the pH of the solution—initially equal to 7.38—decreased to 7.32 and 7.20 for VINPO and VINPO–PTOS, respectively. Solubility results are depicted in Fig. 8.

While a more substantial enhancement might have been expected for this ionic system – given that water weakens ionic bonds and generally promotes salt solubility – the observed results are not unexpected. Certain tosylate salts are known to exhibit low solubility in water or polar solvents, particularly when their counterions have low aqueous affinity or when the salts are highly crystalline. For example, tosylate salts of sorafenib,[34] lumateperone,[35] and suplatast[36] are reported to display limited aqueous solubility. In the present case, the relatively modest solubility enhancement likely reflects both the hydrophobic nature of VINPO and the notable lattice stability of the VINPO–PTOS salt, as indicated by its high melting point, which far exceeds those of the individual components (see Fig. 7).

To evaluate the physical stability of the newly obtained VINPO–PTOS salts, both the crystalline and the amorphous form were stored under controlled dry conditions (0% RH, 20 °C) for three months in a desiccator. PXRD analyses confirmed that both samples remained physically stable over time, with no evidence of salt dissociation into the individual coformers (Fig. S12 for the crystalline solid and Fig. S13 for the amorphous one). Notably, the amorphous salt also showed no signs of recrystallization. These findings suggest that the strong ionic interactions between VINPO and PTOS contribute to the stabilization of both solid forms. In the case of the amorphous form, these interactions appear sufficient to prevent recrystallization of the solid. This stabilization likely stems from reduced molecular mobility, consistent with the high T_g value observed for the amorphous salt.

Under humid conditions (75% RH, 20 °C), the crystalline salt exhibited excellent stability, showing no changes in appearance (color) or solid-state properties. This contrasts with other VINPO salts reported in literature, which tend to dissociate into their parent coformers under similar conditions.[13] Conversely, the amorphous salt was sensitive to humidity, displaying a visible color change from white to

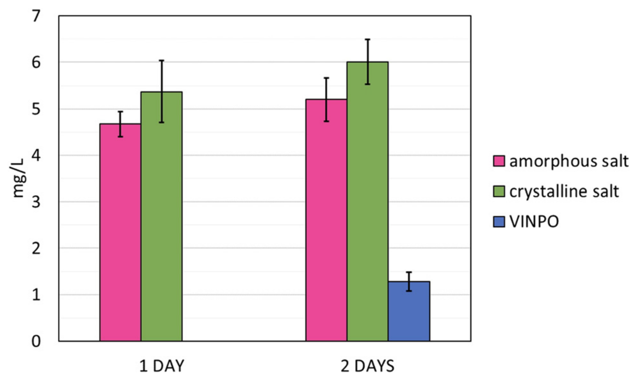

Fig. 8 Solubility VINPO–PTOS crystalline and amorphous salt in comparison to pure VINPO. Please note that pure VINPO reached equilibrium after 2 days, while both amorphous and crystalline salt needed 1 day.

Open Access Article. Published on 20 October 2025. Downloaded on 4/3/2026 6:48:24 AM. This article is licensed under a Creative Commons Attribution-NonCommercial 3.0 Unported Licence.

yellow within just 2 hours of exposure (Fig. S14), followed by recrystallization into the VINPO–PTOS crystalline salt (see Fig. S15 for PXRD analysis), as previously observed during solubility studies. As expected, the amorphous salt adsorbs more water than its crystalline counterpart (as also observed from the TGA results and the ATR spectrum), and this adsorbed moisture acted as a plasticizer, lowering the T_g and accelerating the crystallization process. The yellow coloration, likely due to reversible hydrochromism, was limited to the surface of the powder and disappeared upon manual grinding, reverting the sample to its original white appearance during PXRD preparation.

4. Conclusions

In this work, two novel vinpocetine salts with *p*-toluenesulfonic acid – one crystalline and one amorphous – were successfully obtained through water-assisted or solvent-free mechanochemical approaches. The highly sustainable water-assisted method yielded a stable equimolar salt form, whose crystalline structure was elucidated *via* single-crystal X-ray diffraction, while the amorphous counterpart was characterized and confirmed to retain its ionic nature by XPS analysis. The significant ΔpK_a between vinpocetine and *p*-toluenesulfonic acid was key to promoting salt formation, resulting in strong ionic interactions, as evidenced by thermal and spectroscopic data. Both solid forms displayed enhanced aqueous solubility at physiological temperature, with faster attainment of thermodynamic equilibrium compared to pure vinpocetine under the tested conditions (pH 7.4). In particular, the crystalline salt exhibited excellent thermal and physical stability under both dry and humid conditions, while the amorphous salt, despite its greater hygroscopicity, remained stable under dry storage and showed a tendency to recrystallize into the same crystalline phase upon exposure to moisture or during dissolution.

Author contributions

Ilenia D'Abbrunzo: writing – original draft, investigation, conceptualization. Francesca Beltrame: writing – original draft, investigation. Lara Gigli: software, investigation. Nicola Demitri: software, investigation. Giuseppe Procida: writing – original draft, investigation. Cinzia Cepek: writing – review & editing, resources, methodology. Ferdinando Bassato: writing – review & editing, resources, methodology. Dario Voinovich: writing – review & editing, supervision. Beatrice Perissutti: writing – review & editing, supervision, resources, project administration, conceptualization.

Conflicts of interest

There are no conflicts to declare.

Data availability

Supplementary information (SI): Table S1. Fit XPS (N 1s); Table S2. Fit XPS (C 1s); Table S3. Fit XPS (O 1s); Fig. S1. Visual appearance of VINPO–PTOS salt powders ground (2 h) in the presence of EA (A), ACT (B), ACN (C), MeOH (D), EtOH (E), and H_2O (F); Fig. S2. PXRD pattern of the VINPO–PTOS salt obtained using LAG (2 h) employing different solvents (from top to bottom: HXN, 4-MTHP, EA, ACT, EtOH, MeOH, ACN and H_2O), compared with VINPO and PTOS MH; Table S4. Crystallographic data and refinement details for VINPO–PTOS salt at 298 K and 100 K; Fig. S3. Comparison of the C 1s XPS spectra for pure VINPO (c), the VINPO–PTOS amorphous system (b), and the crystalline (a) VINPO–PTOS salt; Fig. S4. Comparison of the O 1s XPS spectra for pure VINPO (c), the VINPO–PTOS amorphous system (b), and the crystalline (a) VINPO–PTOS salt; Fig. S5. HPLC chromatogram of pure VINPO (yellow), crystalline VINPO–PTOS salt obtained by WAG process (blue) and amorphous VINPO–PTOS salt obtained by NG process (green); Fig. S6. TGA (black) and DSC (red) curves of crystalline VINPO–PTOS salt; Fig. S7. TGA (black) and DSC (red) curves of amorphous VINPO–PTOS salt. Fig. S8. Glass transition temperature (T_g) for the amorphous VINPO–PTOS salt detected in the second heating run (heating/cooling/heating cycle); Fig. S9. Glass transition temperature (T_g) for PTOS MH, detected in the second heating run (heating/cooling/heating cycle); Fig. S10. FT-IR ATR spectra of VINPO–PTOS crystalline (green) and amorphous (pink) salts, compared to VINPO (blue) and PTOS MH (red). Differences between the two salts spectra are highlighted through light grey rectangles; differences with the starting materials are highlighted through light orange rectangles; Fig. S11. PXRD of the white solid collected after solubility studies of (initially) amorphous VINPO–PTOS salt; Fig. S12. Physical stability of VINPO–PTOS crystalline salt over time; Fig. S13. Physical stability of VINPO–PTOS amorphous salt over time; Fig. S14. Appearance of VINPO–PTOS amorphous salt (yellow) and crystalline salt (white) after 2 h of storage at 75% RH and 20 °C; Fig. S15. PXRD of VINPO–PTOS amorphous salt after 2 h of exposure to 75% RH. See DOI: https://doi.org/10.1039/d5pm00225g.

CCDC 2447789 (100 K) and 2447790 (298 K) contain the supplementary crystallographic data for this paper.[37a,b]

Acknowledgements

We thank Serena Bertoni, Giacomo Filippini and Antonella Calabretti for their collaboration and valuable exchange of ideas.

References

1 D. Mori, R. Patel, A. Parmar, A. Patel and M. Patel, *AAPS PharmSciTech*, 2025, **26**, 36.
2 A. T. M. Serajuddin, *Adv. Drug Delivery Rev.*, 2007, **59**, 603–616.

© 2026 The Author(s). Published by the Royal Society of Chemistry

Open Access Article. Published on 20 October 2025. Downloaded on 4/3/2026 6:48:24 AM.
This article is licensed under a Creative Commons Attribution-NonCommercial 3.0 Unported Licence.

3 H. Ueda, W. Wu, K. Löbmann, H. Grohganz, A. Müllertz and T. Rades, *Mol. Pharm.*, 2018, **15**, 2036–2044.

4 H. G. Brittain, *Am. Pharm. Rev.*, 2009, **12**, 117788.

5 A. V. Trask, D. A. Haynes, W. D. S. Motherwell and W. Jones, *Chem. Commun.*, 2006, **7**, 51–53.

6 Á. Vas, B. Gulyás, Z. Szabó, P. Bönöczk, L. Csiba, B. Kiss, E. Kárpáti, G. Pánczél and Z. Nagy, *J. Neurol. Sci.*, 2002, **203–204**, 259–262.

7 Y. Zhang, J. Li and C. Yan, *Eur. J. Pharmacol.*, 2018, **819**, 30–34.

8 Z. C. Dong, Y. Shi, L. J. Liu, T. T. Feng, Y. Zhou and B. W. Pan, *RSC Adv.*, 2024, **14**, 7981–7991.

9 P. Pudleiner and L. Vereczkey, *Eur. J. Drug Metab. Pharmacokinet.*, 1993, **18**, 317–321.

10 Vinpocetine – European Pharmacopoeia 11.6, https://pheur.edqm.eu/app/11-6/content/11-6/2139E.htm?highlight=on&terms%5B%5D=vinpocetine, (accessed March 21, 2025).

11 I. D'Abbrunzo, R. Birolo, M. R. Chierotti, D.-K. Bučar, D. Voinovich, B. Perissutti and D. Hasa, *Eur. J. Pharm. Biopharm.*, 2024, **201**, 114344.

12 S. Golob, M. Perry, M. Lusi, M. R. Chierotti, I. Grabnar, L. Lassiani, D. Voinovich and M. J. Zaworotko, *J. Pharm. Sci.*, 2016, **105**, 3626–3633.

13 Y. Ma, S. Ge, W. Wang, Q. Zheng, Y. Zuo, C. Zhong and B. Sun, *J. Mol. Struct.*, 2016, **1105**, 1–10.

14 D. Hasa, D. Voinovich, B. Perissutti, M. Grassi, A. Bonifacio, V. Sergo, C. Cepek, M. R. Chierotti, R. Gobetto, S. Dall'Acqua and S. Invernizzi, *Pharm. Res.*, 2011, **28**, 1870–1883.

15 M. Arhangelskis, D.-K. Bučar, S. Bordignon, M. R. Chierotti, S. A. Stratford, D. Voinovich, W. Jones and D. Hasa, *Chem. Sci.*, 2021, **12**, 3264–3269.

16 PubChem, *p*-toluenesulfonic acid, https://pubchem.ncbi.nlm.nih.gov/compound/6101, (accessed June 16, 2025).

17 P. Disisto, L. Baraldi, L. Fornasari, I. Bassanetti, V. Mileo, F. Castagnini, F. Ferlenghi, P. Franceschi, A. Bacchi and L. Marchiò, *Eur. J. Pharm. Biopharm.*, 2025, **213**, 114758.

18 Home – The Cambridge Crystallographic Data Centre (CCDC), https://www.ccdc.cam.ac.uk/, (accessed June 1, 2025).

19 A. Lausi, M. Polentarutti, S. Onesti, J. R. Plaisier, E. Busetto, G. Bais, L. Barba, A. Cassetta, G. Campi, D. Lamba, A. Pifferi, S. C. Mande, D. D. Sarma, S. M. Sharma and G. Paolucci, *Eur. Phys. J. Plus*, 2015, **130**, 1–8.

20 B. H. Toby and R. B. Von Dreele, *J. Appl. Crystallogr.*, 2013, **46**, 544–549.

21 W. Kabsch, *Acta Crystallogr., Sect. D: Biol. Crystallogr.*, 2010, **66**, 125–132.

22 P. Emsley, B. Lohkamp, W. G. Scott and K. Cowtan, *Acta Crystallogr., Sect. D: Biol. Crystallogr.*, 2010, **66**, 486–501.

23 S. Parsons, H. D. Flack and T. Wagner, *Acta Crystallogr., Sect. B:Struct. Sci., Cryst. Eng. Mater.*, 2013, **69**, 249–259.

24 L. J. Farrugia, *J. Appl. Crystallogr.*, 2012, **45**, 849–854.

25 C. F. Macrae, I. Sovago, S. J. Cottrell, P. T. A. Galek, P. McCabe, E. Pidcock, M. Platings, G. P. Shields, J. S. Stevens, M. Towler and P. A. Wood, *J. Appl. Crystallogr.*, 2020, **53**, 226–235.

26 I. D'Abbrunzo, E. Venier, F. Selmin, I. Škorić, E. Bernardo, G. Procida and B. Perissutti, *Pharmaceutics*, 2025, **17**, 92.

27 Ö. Karaer, Ş. Dinç-Zor and B. Aşçı, *J. AOAC Int.*, 2022, **105**, 688–695.

28 L. S. S. Ribeiro, D. C. Ferreira and F. J. B. Veiga, *Eur. J. Pharm. Sci.*, 2003, **20**, 253–266.

29 G. Bolla and A. Nangia, *CrystEngComm*, 2018, **20**, 6394–6405.

30 K. K. Sarmah, A. Sarma, K. Roy, D. R. Rao and R. Thakuria, *Cryst. Growth Des.*, 2016, **16**, 1047–1055.

31 L. Yu, *Adv. Drug Delivery Rev.*, 2001, **48**, 27–42.

32 A. Ali, R. Kharshoum and R. Sanad, *Int. J. Drug Delivery*, 2013, **5**, 167–176.

33 S. A. A. A. Hard, H. N. Shivakumar and M. A. M. Redhwan, *Int. J. Biol. Macromol.*, 2023, **253**, 127217.

34 D. H. Truong, T. H. Tran, T. Ramasamy, J. Y. Choi, H.-G. Choi, C. S. Yong and J. O. Kim, *Powder Technol.*, 2015, **283**, 260–265.

35 Lumateperone tosylate-Center For Drug Evaluation And Research Application Number: 209500orig1s000 Product Quality Review, https://www.accessdata.fda.gov/drugsatfda_docs/nda/2019/209500Orig1s000ChemR.pdf (accessed July 16, 2025).

36 Suplatast tosylate-Cayman Chemical product information item No 30316, https://cdn.caymanchem.com/cdn/insert/30316.pdf (accessed July 16, 2025).

37 (*a*) CCDC 2447789: Experimental Crystal Structure Determination, 2025, DOI: 10.5517/ccdc.csd.cc2n53yx; (*b*) CCDC 2447790: Experimental Crystal Structure Determination, 2025, DOI: 10.5517/ccdc.csd.cc2n53zy.

© 2026 The Author(s). Published by the Royal Society of Chemistry